

Cite this: *J. Mater. Chem. C*, 2019,
7, 12263Effect of conjugation length on the properties of
fused perylene diimides with variable isoindigos†Yaping Yu,^a Ning Xue,^b Chengyi Xiao,^b Mahesh Kumar Ravva,^c Yanjun Guo,^a
Liyun Wu,^a Lei Zhang,^b Zhengke Li,^{*a} Wan Yue^{id} ^{*a} and Zhaohui Wang^d

We have successfully synthesized four fused hybrid diimide and diamide arrays with different effective conjugation lengths of perylene diimides and isoindigos. These arrays with varying numbers of amides and imides are an efficient strategy to fine-tune the opto-electronic properties, conformation, energy levels and device performance. It is shown that additional fused isoindigos lead to much lower electron affinity with no influence on the ionic potential. The impact of adding different additional central electron deficient isoindigos to the fused arrays has also been investigated systematically. **PDI-BDOPV-PDI** incorporating a strong electron deficient **BDOPV** unit with enforced coplanarity exhibits a very low lowest unoccupied molecular orbital (LUMO) level of -4.11 eV, and the absorption spectrum of **PDI-DPN-PDI** was even extended to 1000 nm. Thin film transistors were fabricated with these arrays as the semiconductor layers, the fused arrays display electron transport behaviors.

Received 26th July 2019,
Accepted 15th September 2019

DOI: 10.1039/c9tc04078a

rsc.li/materials-c

Introduction

Organic semiconductor materials are widely investigated as they are the key components for organic thin film transistors (OTFTs),¹ organic solar cells,² and organic light emitting diodes.³ The past decades have witnessed the emergence of OTFTs with advantages of flexibility, light-weight and low-cost, making it one of the most promising fields in organic electronics.⁴ To enhance the mobility and stability of OTFT devices, much effort was devoted to the optimization of the molecular backbone structure, film morphology and device structures.⁵ In the exploration of high performance and high stability materials for OTFTs, fused-ring structures proved to be an effective strategy in improving the effective conjugation length and facilitating π -electron delocalization. Meanwhile, the covalently forced planarization of a fused structure can suppress the rotational disorder and lower the reorganization energy, thus increasing the mobility of

OTFT devices.⁶ It is exciting that p-type (hole-transporting) semiconductor materials have flourished with mobility even higher than that of multi-crystalline silicon.⁷ Nevertheless, the n-channel (electron-transport) counterparts obviously lag behind p-type materials, whereas they are necessary for construction of organic p–n junctions and complementary logic circuits.⁸

The incorporation of electron-withdrawing moieties is a very efficient strategy to lower the lowest unoccupied molecular orbital (LUMO) level to facilitate electron injection and transport as well as improve the stability of π -acceptors.⁹ Among the inherently electron deficient π -scaffolds, arylene diimide¹⁰ and arylene diamide¹¹ based π -scaffolds are two versatile functional material systems. Out of the arylene diimides, perylene tetracarboxylic diimides (PDIs) have been developed as promising semiconductor materials due to their strong electron deficient character and high stability.¹² Particularly **PDI** small molecules have been considered as better alternatives to fullerenes for organic electronics.¹³ Isoindigo (**IID**) is also a well-studied arylene diamide material system due to its two electron deficient lactams and photostability.¹⁴ Alkyl chain functionalization at the nitrogen atoms of both **PDI** and **IID** can easily regulate the solubility and packing of the resulting materials. Kelly *et al.* reported several different length and planarity **IID** acceptor units and their effect on the optoelectronic properties of **IID** polymers.¹⁵ The fusion of **PDI** with other building blocks to form larger conjugation skeletons has become an efficient strategy to develop novel organic electron transporting materials. Fusing **PDI** with truxene and fluorene cores can afford novel star-shaped molecules Tr-PBI and TetraPDI-PF respectively.^{16,17} However, the construction of elongated fused electron deficient π -acceptors remains highly

^a Key Laboratory for Polymeric Composite and Functional Materials of Ministry of Education, School of Materials and Engineering, Sun Yet-Sen University, Guangzhou 510275, China. E-mail: lizhengke@mail.sysu.edu.cn, yuew5@mail.sysu.edu.cn

^b College of Energy, Beijing University of Chemical Technology, Beijing 100029, China

^c Department of Chemistry, SRM University – AP, Amaravati 522502, India

^d Key Laboratory of Organic Optoelectronics and Molecular Engineering, Department of Chemistry, Tsinghua University, Beijing 100084, China

† Electronic supplementary information (ESI) available: Experimental details, DFT results, syntheses of materials, complete characterization of materials, device characterization and XRD results. Syntheses of monomers, complete characterization of materials, transfer and output curves of materials. See DOI: 10.1039/c9tc04078a

challenging owing to the tediousness of synthetic chemistry and poor solubility of the products, mainly due to the reduced chemical reactivity of the electron deficient building blocks and/or steric hindrance of these electron-deficient substituents.^{10b} Hence it remains essential to develop electron-deficient fused π -scaffolds to lead n-type material innovation. We are particularly interested in the molecular engineering of electron deficient **IID** core modification.¹⁸ Meanwhile, systematic work about rylene dyes as exceptional high-performance n-channel semiconductors in organic field-effect transistors (OFETs) and competitive candidates for non-fullerene acceptors in high efficiency organic photovoltaic devices (OPVs) has also reported by us.^{10c,13} One typical example is hybrid fused **PDI** and naphthalene tetracarboxylic diimide (**NDI**) arrays, which possessed bathochromically shifted absorption as well as high electron affinities (EAs) up to 4.2 eV, and one of the arrays exhibited air-stable electron transport behavior.¹⁹ These achievements motivate us to continue to study fused hybrid imide and amide systems.

Herein, we report a series of fused hybrid **PDI** and variable **IID** arrays with different conjugation length. These fused arrays show fine-tunable absorption properties, conformation and energy levels due to the effective communication and charge delocalization between the diimide and diamide units. When utilized as the active layers of OTFTs, the arrays exhibit encouraging electron mobility under a nitrogen atmosphere.

Experimental

Materials and measurements

¹H NMR and ¹³C NMR spectra were recorded in deuterated solvents on a Bruker AVANCE 400 NMR spectrometer and a Bruker AVIII 500WB NMR spectrometer. ¹H NMR chemical shifts are reported in ppm downfield from the tetramethylsilane (TMS) reference using the residual protonated solvent as an internal standard. Mass spectra (MALDI-TOF-MS) were measured on a Bruker BIFLEX III mass spectrometer. Absorption spectra were measured with a Hitachi (model U-3010) UV-vis spectrophotometer in a 1 cm quartz cell. Cyclic voltammetry (CV) and differential pulse voltammetry (DPV) were performed with a Zahner IM6e electrochemical workstation using glassy carbon discs as the working electrode, Pt wire as the counter electrode, and a Ag/AgCl electrode as the reference electrode. 0.1 M tetrabutylammoniumhexafluorophosphate (Bu₄NPF₆) dissolved in CH₂Cl₂ (**PDI-IID-PDI**) or *o*-dichlorobenzene (**PDI-IID**, **PDI-BDOPV-PDI**, and **PDI-DPN-PDI**) was employed as the supporting electrolyte with a scan rate of 100 mV s⁻¹. The plot includes the signal of ferrocene as an internal potential marker. CH₂Cl₂ was freshly distilled prior to use. The intramolecular dehydrogenation to obtain **PDI-IID-PDI** was performed with a LED flow reactor WP-VLH-1020 (WATTCAS). X ray diffraction (XRD) was performed on a D/max2500 with a CuK α source ($\kappa = 1.541 \text{ \AA}$).

DFT methodology

Geometries were fully optimized at the B3LYP/6-31G(d,p) level of theory. The long alkyl side-chains were replaced by methyl

groups to reduce computational costs. The range-separation parameter (ω) was optimized for each molecule using the IP-tuning method; the optimal ω value for the **IID**, **PDI**, **PDI-IID**, **PDI-IID-PDI**, **PDI-BDOPV-PDI**, and **PDI-DPN-PDI** molecules consider in the study is respectively 0.023, 0.018, 0.012, 0.008, 0.008, and 0.01 Bohr⁻¹. Vertical ionization potentials and electron affinities were calculated at the PCM (chloroform)-OT- ω B97XD/6-31G(d,p) level of theory using the ground-state (S₀) geometries. Excited state energies were calculated using the TDDFT method at the PCM (chloroform)-OT- ω B97XD/6-31G(d,p) level of theory. Natural transition orbital analyses were also carried out to characterize the nature of the excited state. All calculations were carried out with the Gaussian 16 package.

Device fabrication

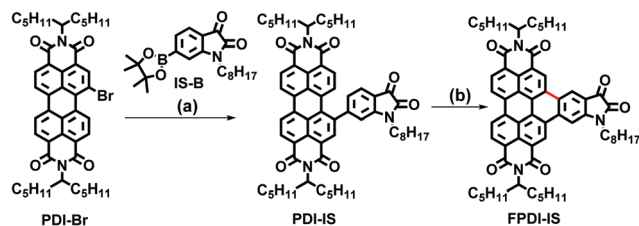
The gate electrode and dielectric layer were fabricated from a heavily doped Si wafer and 300 nm SiO₂, respectively. Source/drain Au electrodes were sputtered and patterned by a lift-off technique. The SiO₂/Si wafers used here were cleaned consecutively with deionized water, piranha solution (H₂SO₄/H₂O₂ = 2 : 1), deionized water, and isopropyl alcohol, and finally were blown dry with high-purity nitrogen gas. Octadecyltrichlorosilane (OTS) modified substrates were produced with the vapor-deposition method: the cleaned wafers were dried under a vacuum at 90 °C for 0.5 h to eliminate moisture. When the temperature decreased to 70 °C, a small drop of OTS was dropped onto the wafers. Subsequently, this system was heated to 120 °C for 2 h under a vacuum. The OTS modified substrates used here were cleaned with *n*-hexane, chloroform and isopropyl alcohol in sequence, and finally were blown dry with high-purity nitrogen gas.

Films of the semiconductors were spin-coated from solution (10 mg mL⁻¹) onto substrates modified with OTS. All devices were measured in an inert atmosphere with a Bottom-Gate Bottom-Contact configuration. The electrical characteristics of the devices were recorded with a Keithley 4200-SCS semiconductor parameter analyser and a Micromanipulator 6150 probe station in a glove box at room temperature.

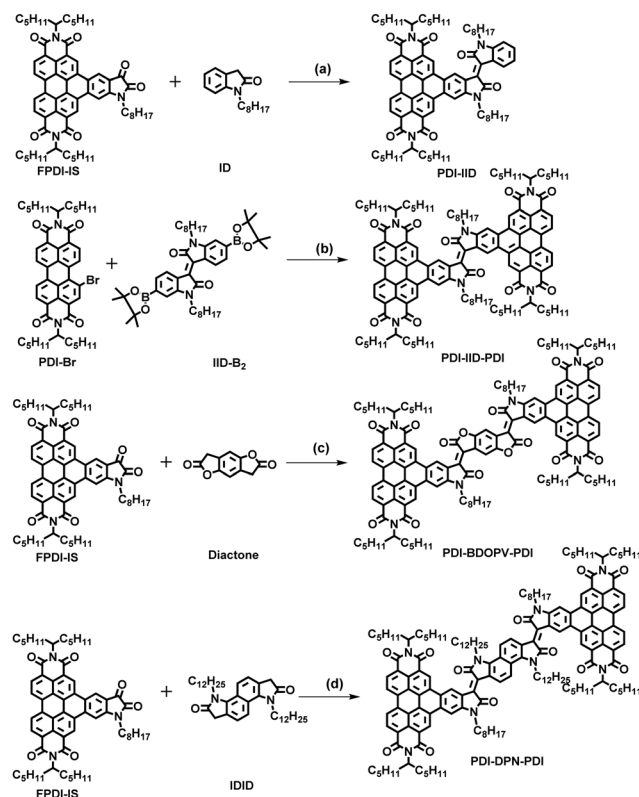
Results and discussion

Synthetic procedures

The synthetic procedures for our fused arrays are depicted in Schemes 1 and 2. Mono bromo *N,N'*-di(6-undecyl)perylene diimide (**PDI-Br**) was chosen as the starting material for our fused system;²⁰ the branched 6-undecyl was attached to endow the resulting fused π -system with good solubility. Pd-catalysed Miyaura borylation between 6-bromo-isatin and bis(pinacolato)-diboron furnished 6-boreaster isatin (**IS-B**) in an excellent yield,²¹ followed by another Suzuki cross coupling between **PDI-Br** and **IS-B** to afford crude intermediate **PDI-IS** without further characterization, which can go through a ring-closing reaction immediately in the air. Last, intramolecular dehydrogenation induced by natural light successfully provided our fused **PDI** and isatin **FPDI-IS** in a good yield through the two steps (Scheme 1).



Scheme 1 Synthetic route of FPDI-IS: (a) $\text{Pd}_2(\text{dba})_3$, $\text{P}(\text{t-Bu})_3\cdot\text{HBF}_4$, K_3PO_4 , THF, 80 °C, 12 h; (b) I_2 , natural light/air, CHCl_3 , 25 °C, 24 h, 60%.



Scheme 2 The synthetic route of **PDI-IID**, **PDI-IID-PDI**, **PDI-BDOPV-PDI**, and **PDI-DPN-PDI** arrays: (a) AcOH , HCl , 118 °C, 30 h, 87%; (b) $\text{Pd}_2(\text{dba})_3$, $\text{P}(\text{t-Bu})_3\cdot\text{HBF}_4$, K_3PO_4 , THF, 80 °C, 12 h, then I_2 , blue light (450 nm)/air, toluene, 90 °C, 12 h, 65%; (c) PTSA , H_2O , P_2O_5 , toluene, 115 °C, 48 h, 47%; (d) $\text{PTSA}\cdot\text{H}_2\text{O}$, P_2O_5 , toluene, 115 °C, 48 h, 41%.

With the key intermediate **FPDI-IS** in hand, we tried to construct different conjugation length fused systems with different **PDI/IID** ratios (Scheme 2). *N*-Octyl oxindole (**ID**) was synthesized by the reduction of isatin according to the literature.²² *p*-Toluene sulfonic acid monohydrate (PTSA) catalyzed dehydration condensation in the presence of phosphorus pentoxide (P_2O_5) between **PDI-IS** and **ID** to afford **PDI-IID** in a good yield of 87%. Encouraged by the success of this annulation, more fused arrays with π -extended **PDI** and **IID** are expected. **IID-B₂** was provided by the Suzuki coupling of dibromo isoindigo with bis(pinacolato)diboron in an excellent yield,²³ followed by Suzuki cross coupling of **PDI-Br** and **IID-B₂** to afford the single bond linked intermediate. Several ring-closing reaction conditions were used to try to obtain the critical fused-ring product from the

single bond linked intermediate. For example, no product has been detected during the reaction by employing an excess of ferric chloride (FeCl_3) or 2,3-dichloro-5,6-dicyanobenzoquinone (**DDQ**) as an oxidation reagent. Finally, we conducted this dehydrogenation with the assistance of blue light of 450 nm, and the desired product **PDI-IID-PDI** was obtained successfully with a good yield of 65% in two steps; the mechanism of this photo-induced cyclic aromatization has been described in the literature.²⁴ Benzodifurandione based polymers displays high electron mobilities up to $1.1 \text{ cm}^2 \text{ V}^{-1} \text{ s}^{-1}$ under ambient conditions.²⁵ Kelly *et al.* reported a new isoindigo acceptor: bisisoindigo (**BIID**), an isoindigo dimer in which the two phenyl rings are fused across the 6 and 7 positions; the coplanarity substantially reduced the optical band gap relative to that of isoindigo.²⁶ These interesting physicochemical properties and encouraging device performance encourage us to incorporate these versatile and different conjugation length electron poor acceptor units into our **PDI** system to further investigate their opto-electronic properties. Benzodifurandione was prepared according to ref. 25 and bisoxindole with a linear dodecyl chain was synthesized from the reduction of the precursor bisatin in the presence of hydrazine hydrate.²⁷ Expectedly, aldol coupling of **FPDI-IS** and benzodifurandione or bisoxindole with PTSA provides **PDI-BDOPV-PDI** and **PDI-DPN-PDI** in good yields. The details of the synthesis and characterization of the precursors, intermediates and the final fused arrays are given in the ESI.† All these fused arrays exhibit certain solubility in common organic solvents such as chloroform, toluene and chlorobenzene, providing us with the opportunity to perform solution processing of the arrays to prepare thin film devices. All the new compounds were characterized by high-resolution mass spectrometry (**HRMS**), and room-temperature or high-temperature ^1H NMR. Despite good solubility, no obvious proton peaks of the fused arrays at room temperature could be observed in CDCl_3 due to the very strong aggregation for these large aromatic systems.

These four arrays have different effective conjugation length. Of these four arrays, **PDI-IID** and **PDI-IID-PDI** differ from each other in the **PDI/IID** ratio. **PDI-IID** exhibits the smallest conjugation length with one **PDI** fused with one **IID**. For **PDI-IID-PDI**, the conjugation length was enlarged with two **PDI**s fused with one **IID**. For **PDI-IID-PDI**, **PDI-BDOPV-PDI**, and **PDI-DPN-PDI**, which can be considered as two **PDI**s with fused additional different conjugation length and electron-effect **IIDs** into the central of **PDI**s. **PDI-DPN-PDI** can also be regarded as two dimers of **PDI-IID** with enforced coplanarity. The difference in the **PDI/IID** ratio and conjugation structure range will result in significant differences in physicochemical properties and device performance.

Density functional theory (**DFT**) calculations were also carried out to offer an insight into the structural and conformation properties. All optimized structures are depicted in Fig. 1. The long alkyl side-chains were replaced with methyl groups to reduce the computational cost. It can be seen from Fig. 1 that in all compounds, the dihedral angles between adjacent aromatic units (between the two lactam cores) are very small indeed (on the order of 5–15°), a feature previously observed for isoindigo units.²⁸ The reason for twisting in the dihedral angle is due to the presence of

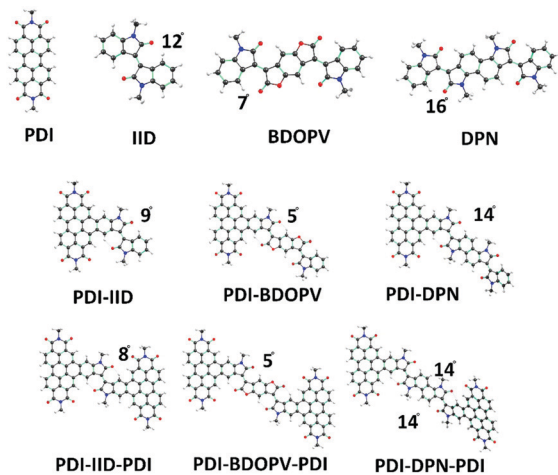


Fig. 1 Optimized geometries of **PDI**, **IID**, **BDOPV**, **DPN**, **PDI-IID**, **PDI-IID-PDI**, **PDI-BDOPV-PDI**, and **PDI-DPN-PDI** as obtained at the ω B97XD/6-31G** level of theory. The torsional angle (in degrees) between units is also given.

steric interaction between a C–H group and an adjacent oxygen atom of the carboxyl group.

Opto-electronic properties

To further understand the structure–optical property relationship of these compounds, the optical properties of these arrays are characterized by UV-vis-NIR absorption spectroscopy. The absorption spectra of isolated **PDI** and **IID** in the solution phase are depicted in Fig. S1 and S2 (ESI†). The isolated **PDI** core exhibits the longest wavelength absorption maximum at 525 nm (Table 1). The isolated **IID** ring exhibits two absorption peaks, with a broad absorption peak at 500 nm and an intense high-energy band. The four fused arrays exhibit broad and strong absorption spectra in the UV-visible range and the absorption spectrum of **PDI-DPN-PDI** even extends to the near infrared (NIR) region. Of the four compounds, the absorption maximum of **PDI-IID** is 460 nm ($\epsilon = 80\,119\text{ M}^{-1}\text{ cm}^{-1}$) and that of **PDI-IID-PDI** is 489 nm ($\epsilon = 90\,645\text{ M}^{-1}\text{ cm}^{-1}$). Obviously, this red shift of **PDI-IID-PDI** can be attributed to the extended π conjugation length compared with that of **PDI-IID**. Variation of the fused central units has a notable impact on the absorption profiles of the arrays. The whole spectra of **PDI-BDOPV-PDI** and **PDI-DPN-PDI** are further significantly bathochromically shifted with low-energy absorption maxima of 602 nm and 768 nm.

The obviously red-shifted and NIR absorption of **PDI-DPN-PDI** can also be attributed to the extended effective conjugation length and increased molecular orbital overlap between the HOMO and LUMO of the aromatic systems. Compared to their absorption spectra in solution, the absorption of all arrays in films with the highest intensity is red-shifted by 4–9 nm, suggesting that the aggregation of these materials in films is stronger than that in solution. The onset absorption of **PDI-IID**, **PDI-IID-PDI**, **PDI-BDOPV-PDI**, and **PDI-DPN-PDI** is at 618 nm, 608 nm, 722 nm and 946 nm, respectively, by which their optical bandgaps can be estimated to be 2.01 eV, 2.04 eV, 1.72 eV and 1.31 eV, respectively (Fig. 2).

Time-dependent DFT calculations (TD-OT- ω B97XD/6-31G** level of theory) were carried out to elucidate the absorption properties of these molecules (Table S1, ESI†). The calculated vertical transition energies of the **PDI** and **IID** cores are in good agreement with the trends obtained from previous experimental and theoretical results. Natural Transition Orbital (NTO) analysis reveals that the lowest optical transition in the isolated **PDI** core is purely local excitation at 525 nm.²⁹

In the case of the isolated **IID** core the lowest optical transition has a partial charge-transfer character (from phenyl rings to core lactam rings, see Fig. S3, ESI†). An analysis of the natural transition orbitals involved in the lowest optical transition, which are illustrated in Fig. S7 (ESI†), indicates that in the cases of **PDI-IID** and **PDI-IID-PDI**, the hole wavefunction is delocalized on the whole molecule whereas the electron wavefunction is localized on **PDI** and **IID** in **PDI-IID** and **PDI-IID-PDI**, respectively. In molecule **PDI-BDOPV-PDI**, the lowest excitation calculated at 670 nm (the experimental value is 722 nm) shows a charge-transfer character (hole localized on the **PDI** cores and electron localized on the central **IID** core).

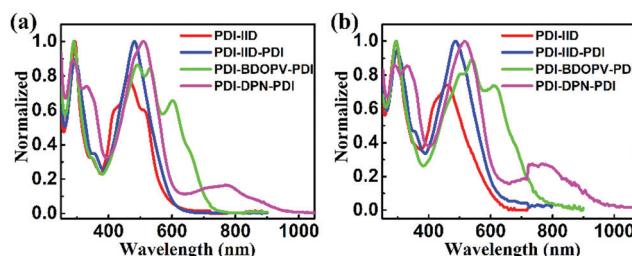


Fig. 2 Absorption spectra of **PDI-IID**, **PDI-IID-PDI**, **PDI-BDOPV-PDI**, and **PDI-DPN-PDI** in solution (a) and in thin films as cast from toluene solution (b).

Table 1 Opto-electronic properties of the **PDI**, **IID** and fused arrays

Compound	λ_{peak}^a [nm]	ϵ^b [$\text{M}^{-1}\text{ cm}^{-1}$]	λ_{onset}^c [nm]	E_{1r}^d [eV]	E_{opt}^e [eV]	LUMO ^f [eV]	HOMO ^g [eV]
PDI	458, 490, 525	85 444	547	−1.08	2.27	−3.72	−5.99
IID	394, 500	12 736	623	−1.35	2.00	−3.45	−5.45
PDI-IID	420, 460, 511	80 119	618	−1.23	2.01	−3.57	−5.58
PDI-IID-PDI	481	90 645	608	−1.07	2.04	−3.73	−5.77
PDI-BDOPV-PDI	491, 532, 602	86 698	722	−0.69	1.72	−4.11	−5.83
PDI-DPN-PDI	519, 768	93 526	946	−1.06	1.31	−3.74	−5.05

^a The absorption peaks of the fused arrays. ^b The molar extinction coefficient of compounds with the highest absorption intensity. ^c Calculated by the onset of solution absorption spectra of the arrays. ^d Calculated from the first half reduction potentials of cyclic voltammetry (in V vs. Fc/Fc⁺). ^e Estimated by $1240/\lambda_{\text{onset}}$. ^f Estimated using $\text{LUMO} = -(4.8 + E_{1r})$. ^g $\text{HOMO} = \text{LUMO} - E_{\text{opt}}$.

For molecule **PDI-DPN-PDI**, the lowest excitation calculated at 850 nm (the experimental value is 946 nm) is predominantly a HOMO \rightarrow LUMO transition; the corresponding NTOs have character similar to the molecular orbital wave-function distributions depicted in Fig. S4 (ESI †). The high-energy absorption in these four molecules is characterized as local excitations as both the hole and electron wavefunctions reside within the same spatial extent of the molecule, though there is a partial charge-transfer-like character in some molecules (Fig. S8–S12, ESI †).

Cyclic voltammetry was utilized to estimate the redox properties and energy levels of these arrays, which are also summarized in Table 1. **PDI**, **IID** and our arrays all exhibit reversible reduction potentials owing to their electron acceptor character (Fig. 3 and Fig. S1, ESI †). The onset of the first reduction potentials of the compounds is -1.08 eV for **PDI**; -1.35 eV for **IID**; -1.23 eV for **PDI-IID**; -1.07 eV for hybrid **PDI-IID-PDI**; -0.69 eV for **PDI-BDOPV-PDI**, and -1.06 eV for **PDI-DPN-PDI**. Differential pulse voltammetry was also conducted for **PDI-BDOPV-PDI** and **PDI-DPN-PDI** to confirm their multi-electron reduction ability (Fig. S13, ESI †). The LUMO levels of these arrays are -3.57 eV for **PDI-IID**, -3.73 eV for **PDI-IID-PDI**, -4.11 eV for **PDI-BDOPV-PDI**, and -3.74 eV for **PDI-DPN-PDI**. Further, to gain knowledge of the redox properties of these molecules, DFT calculations at the B3LYP/6-31G(d,p) level of theory on the optimized geometries were performed. Fusion of the **IID** ring at the bay position of the **PDI** core results in the **PDI-IID** molecule in which the HOMO is well-delocalized over the entire skeleton whereas the LUMO is mainly localized on the **PDI** core (see Fig. S1, ESI †). Addition of another **PDI** core to **PDI-IID** gives **PDI-IID-PDI** where the LUMO wavefunction is fully delocalized over the entire molecule. Pictorial representations of the HOMO and LUMO wavefunctions are shown in Fig. S4 (ESI †). It can be seen from Fig. S5 (ESI †) that fusion of **PDI** and **BDOPV** molecules results in **PDI-BDOPV** whose HOMO wavefunction is delocalized over the entire skeleton whereas

the LUMO is predominantly localized on the **BDOPV** unit. Further addition of another **PDI** unit to **PDI-BDOPV** results in the **PDI-BDOPV-PDI** molecule wherein the LUMO value is much lower than the isolated **BDOPV** and **PDI-BDOPV** molecules. In the case of molecule **PDI-DPN-PDI**, both the HOMO and LUMO wavefunctions are localized mainly on the central core unit. But, the much lower LUMO of **PDI-BDOPV-PDI** (-3.82 eV) than that of **PDI-DPN-PDI** (-3.55 eV) indicates the stronger electron deficient property of the central **BDOPV** than that of the **DPN** part. The LUMO and HOMO values of these arrays are in good agreement with the calculated DFT calculation data (Table 1 and Fig. S6, ESI †). The ratio of **PDI/IID** led to different conjugation lengths in the molecules accompanied by large change in the HOMO and LUMO energy levels (Fig. 4).

Device characterization

To gain the effect of the different conjugated fused arrays on the charge carrier mobilities, the arrays were used to fabricate bottom-gate bottom-contact (BGBC) OFETs. A concentration of 10 mg mL^{-1} in solution on octyltrichlorosilane (OTS)-treated Si/SiO $_2$ substrates was used for solution processing spin coating of the films for OFETs. The fabrication and evaluation were conducted under a nitrogen atmosphere. **PDI-IID-PDI**, **PDI-BDOPV-PDI** and **PDI-DPN-PDI** display electron transport behaviours due to their relatively low LUMOs. The electron mobilities of the four compounds as a function of different

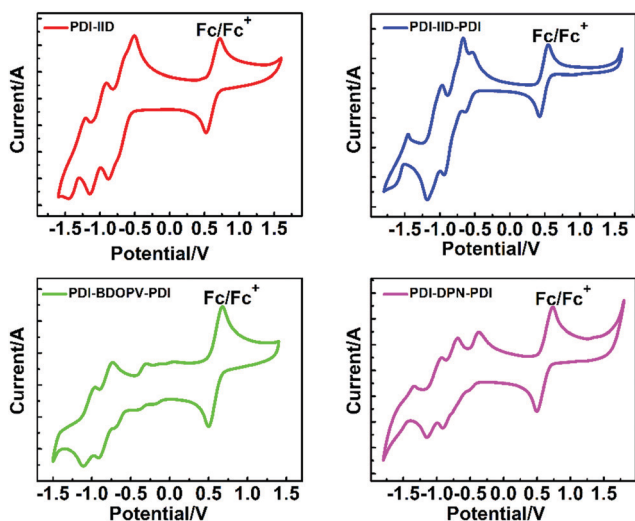


Fig. 3 Reductive cyclic voltammetry of **PDI-IID**, **PDI-IID-PDI**, **PDI-BDOPV-PDI** and **PDI-DPN-PDI**.

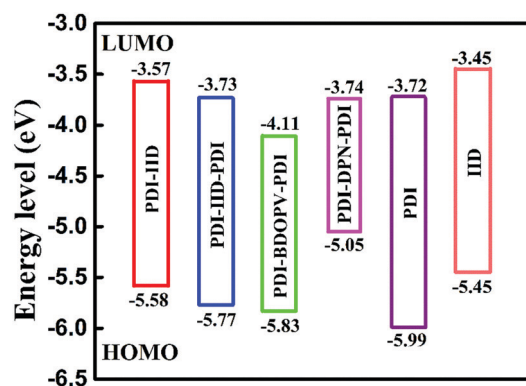


Fig. 4 HOMO and LUMO levels of **PDI**, **IID** and the fused arrays.

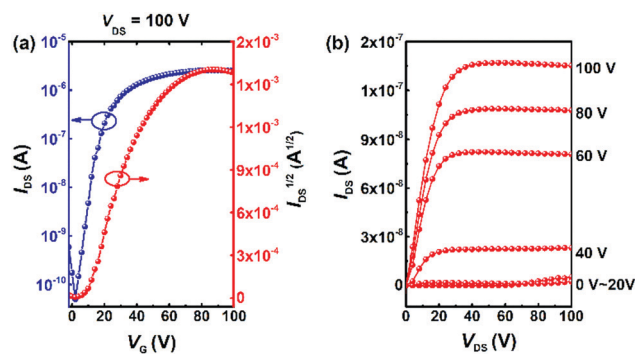


Fig. 5 Transfer (a) and output curves (b) obtained from BGBC OTFTs based on **PDI-DPN-PDI**.

Table 2 Field effect thin film transistor data of compounds in a BGBC configuration

Compound	Solvent	AT ^a [°C]	μ_e max [cm ² V ⁻¹ s ⁻¹]	μ_e ave ^b [cm ² V ⁻¹ s ⁻¹]	V _T ^c [V]	I _{on} /I _{off} ^d
PDI-IID-PDI	Chloroform	60	9.14×10^{-3}	$(6.31 \pm 0.9) \times 10^{-3}$	4.0	2×10^6
PDI-BDOPV-PDI	Toluene	130	2.42×10^{-3}	$(1.36 \pm 0.6) \times 10^{-3}$	-2.5	8×10^5
PDI-DPN-PDI	Toluene	110	1.36×10^{-2}	$(1.14 \pm 0.3) \times 10^{-2}$	8.3	5×10^4

^a Optimized annealing temperature for 30 min before measurement. ^b Electron mobility, each based on 10 devices, all devices were measured under a nitrogen atmosphere. ^c Threshold voltage. ^d On/off current ratio.

annealing temperature are summarized in Table S2 (ESI[†]). Representative transfer and output curves of OFETs of the arrays are shown in Fig. 5 and Fig. S14 (ESI[†]). However, the output curve of **PDI-IID** cannot be obtained, possibly due to the poor contact between the semiconductor and the electrodes. The highest mobility of **PDI-IID-PDI** is 9.14×10^{-3} cm² V⁻¹ s⁻¹ with a current on/off ratio of 2×10^6 and a threshold voltage of 4.0 V. The saturation mobility extracted from the transfer curves of OFETs for **PDI-BDOPV-PDI** is 2.42×10^{-3} cm² V⁻¹ s⁻¹ with a current on/off ratio of 8×10^5 and a threshold voltage of -2.5 V (Table 2). Of all four arrays, **PDI-DPN-PDI** exhibits the highest electron mobility of 1.36×10^{-2} cm² V⁻¹ s⁻¹ with a current on/off ratio of 5×10^4 and a threshold voltage of 8.3 V. To further understand the different molecular packing of these four molecules, X-ray diffraction (XRD) measurements of the thin films with the optimized device conditions were conducted (Fig. S15 and Table S3, ESI[†]). **PDI-IID**, **PDI-BDOPV-PDI** and **PDI-DPN-PDI** exhibit obvious (100) diffraction peaks at $2\theta \approx 4.12^\circ$, 3.88° and 3.82° respectively, indicating strong lamellar stacking with a *d* spacing distance of 21.4 Å, 22.7 Å and 23.2 Å respectively. However, no diffraction peak was observed for the **PDI-IID-PDI** films, indicating the thin film of **PDI-IID-PDI** exhibited an amorphous state. The mobility improvement of **PDI-DPN-PDI** may be due to changes in the packing induced by the extended conjugation length. The different electron transport ability of these arrays demonstrates that fusing additional acceptor units onto the central PDIs can systematically tune the electron mobilities.

Conclusions

In conclusion, we have designed and synthesized a new class of fused hybrid π -conjugated perylene diimide and isoindigo diamides with different conjugation length, **PDI/IID** ratio and planarity effectively. The effect of the conjugation length and **PDI/IID** ratio on the opto-electronic properties and the OFET device performance of the fused diimides and diamides has been investigated systematically with experiment and theory. We found that an extended conjugation length and addition of electron-withdrawing groups can increase the LUMO levels to facilitate electron injection and transport. Our work also highlights the impact of adding additional central electron acceptor diamides to the fused arrays. These central diamides can not only influence the absorption spectra and molecular conformation greatly but also have a pronounced effect on the energy levels and further on the device performance. Our results provide an interesting structure–property relationship of these

fused arrays. We believe that changing the conjugation length and the central electron acceptor can be used as a general strategy to tune rationally the properties of hybrid fused systems.

Conflicts of interest

The authors declare no conflict of interest.

Acknowledgements

The authors thank NSF of China (Grant No. 21875291 and 21702240) for the financial support. MKR thanks SRM Super-computer Centre, SRM Institute of Science and Technology for providing the computational facility.

Notes and references

- H. Dong, X. Fu, J. Liu, Z. Wang and W. Hu, *Adv. Mater.*, 2013, **25**, 6158–6183; H. Klauk, *Organic Electronics: Materials, Manufacturing and Applications*, Wiley-VCH, Germany, 2006.
- Y. Lin, Y. Li and X. Zhan, *Chem. Soc. Rev.*, 2012, **41**, 4245–4272.
- C. Sekine, Y. Tsubata, T. Yamada, M. Kitano and S. Doi, *Sci. Technol. Adv. Mater.*, 2014, **3**, 034203.
- H. Sirringhaus, *Adv. Mater.*, 2014, **26**, 1319–1335.
- C. Wang, H. Dong, W. Hu, Y. Liu and D. Zhu, *Chem. Rev.*, 2012, **112**, 2208–2267.
- J.-S. Wu, S.-W. Cheng, Y.-J. Cheng and C.-S. Hsu, *Chem. Soc. Rev.*, 2015, **44**, 1113–1154.
- T. Kazuo, O. Itaru, M. Takamichi and N. Masahiro, *Acc. Chem. Res.*, 2014, **47**, 1493–1502.
- Y. Zhao, Y. Guo and Y. Liu, *Adv. Mater.*, 2013, **25**, 5372–5391.
- (a) S. Chen, Y. Zhao, A. Bolag, J.-I. Nishida, Y. Liu and Y. Yamashita, *ACS Appl. Mater. Interfaces*, 2012, **4**, 3994–4000; (b) Y. Sakamoto, T. Suzuki, M. Kobayashi, Y. Gao, Y. Fukai, Y. Inoue, F. Sato and S. Tokito, *J. Am. Chem. Soc.*, 2004, **126**, 8138–8140.
- (a) H. Li, Y. J. Hwang, B. A. Courtright, F. N. Eberle, S. Subramanian and S. A. Jenekhe, *Adv. Mater.*, 2015, **27**, 3266–3272; (b) Y. Wang, H. Guo, S. Ling, I. Arrechea-Marcos, Y. Wang, J. T. López Navarrete, R. P. Ortiz and X. Guo, *Angew. Chem., Int. Ed.*, 2017, **56**, 9924–9929; (c) W. Jiang, Y. Li and Z. Wang, *Acc. Chem. Res.*, 2014, **47**, 3135–3147.
- (a) R. Stalder, J. Mei, K. R. Graham, L. A. Estrada and J. R. Reynolds, *Chem. Mater.*, 2014, **26**, 664–678; (b) C. B. Nielsen, M. Turbiez and I. McCulloch, *Adv. Mater.*, 2013, **25**,

- 1859–1880; (c) X. Guo, A. Facchetti and T. J. Marks, *Chem. Rev.*, 2014, **114**, 8943–9021.
- 12 (a) F. Würthner and M. Stolte, *Chem. Commun.*, 2011, **47**, 5109–5115; (b) X. Zhan, J. Zhang, S. Tang, Y. Lin, M. Zhao, J. Yang, H.-L. Zhang, Q. Peng, G. Yu and Z. Li, *Chem. Commun.*, 2015, **51**, 7156.
- 13 (a) A. Nowak-Król, K. Shoyama, M. Stolte and F. Würthner, *Chem. Commun.*, 2018, **54**, 13763; (b) D. Meng, G. Liu, C. Xiao, Y. Shi, L. Zhang, L. Jiang, K. K. Baldridge, Y. Li, J. S. Siegel and Z. Wang, *J. Am. Chem. Soc.*, 2019, **141**, 5402–5408; (c) D. Meng, H. Fu, C. Xiao, X. Meng, T. Winands, W. Ma, W. Wei, B. Fan, L. Huo, N. L. Doltsinis, Y. Li, Y. Sun and Z. Wang, *J. Am. Chem. Soc.*, 2016, **138**, 10184–10190.
- 14 E. Wang, W. Mammo and M. R. Andersson, *Adv. Mater.*, 2014, **26**, 1801–1826.
- 15 N. M. Randell, C. L. Radford, J. Yang, J. Quinn, D. Hou, Y. Li and T. L. Kelly, *Chem. Mater.*, 2018, **30**, 4864–4873.
- 16 Y. Xie, X. Zhang, Y. Xiao, Y. Zhang, F. Zhou, J. Qi and J. Qu, *Chem. Commun.*, 2012, **48**, 4338–4340.
- 17 Y. Zhang, L. Chen, K. Zhang, H. Wang and Y. Xiao, *Chem. – Eur. J.*, 2014, **20**, 10170–10178.
- 18 (a) R. S. Ashraf, A. J. Kronemeijer, D. I. James, H. Sirringhaus and I. McCulloch, *Chem. Commun.*, 2012, **48**, 3939–3941; (b) I. Meager, M. Nikolka, B. C. Schroeder, C. B. Nielsen, M. Planells, H. Bronstein, J. W. Rumer, D. I. James, R. S. Ashraf, A. Sadhanala, P. Hayoz, J.-C. Flores, H. Sirringhaus and I. McCulloch, *Adv. Funct. Mater.*, 2014, **24**, 7109–7115; (c) W. Yue, R. S. Ashraf, C. B. Nielsen, E. Collado-Fregoso, M. R. Niazi, S. A. Yousaf, M. Kirkus, H.-Y. Chen, A. Amassian, J. R. Durrant and I. McCulloch, *Adv. Mater.*, 2015, **27**, 4702–4707; (d) W. Yue, M. Nikolka, M. Xiao, A. Sadhanala, C. B. Nielsen, A. J. P. White, H.-Y. Chen, A. Onwubiko, H. Sirringhaus and I. McCulloch, *J. Mater. Chem. C*, 2016, **4**, 9704–9710.
- 19 W. Yue, A. Lv, J. Gao, W. Jiang, L. Hao, C. Li, Y. Li, L. E. Polander, S. Barlow, W. Hu, S. D. Motta, F. Negri, S. R. Marder and Z. Wang, *J. Am. Chem. Soc.*, 2012, **134**, 5770–5773.
- 20 P. Rajasingh, R. Cohen, E. Shirman, L. J. W. Shimon and B. J. Rybtchinski, *J. Org. Chem.*, 2007, **72**, 5973–5979.
- 21 H. Liao, C. Xiao, M. K. Ravva, Y. Wang, M. Little, M. V. C. Jenart, A. Onwubiko, Z. Li, Z. Wang, J.-L. Brédas, I. McCulloch and W. Yue, *Chem. Commun.*, 2018, **54**, 11152.
- 22 J.-L. Li, Y.-F. Chai, W. V. Wang, Z.-F. Shi, Z.-G. Xu and H.-L. Zhang, *Chem. Commun.*, 2017, **53**, 5882–5885.
- 23 X. Sun, W. Chen, Z. Du, X. Bao, G. Song, K. Guo, N. Wang and R. Yang, *Polym. Chem.*, 2013, **4**, 1317–1322.
- 24 W. H. Laarhoven, T. H. J. H. M. Cuppen and R. J. F. Nivard, *Tetrahedron*, 1970, **26**, 4865–4881.
- 25 T. Lei, J.-H. Dou, X.-Y. Cao, J.-Y. Wang and J. Pei, *J. Am. Chem. Soc.*, 2013, **135**, 12168–12171.
- 26 N. M. Randell, P. C. Boutin and T. L. Kelly, *J. Mater. Chem. A*, 2016, **4**, 6940–6945.
- 27 A. Onwubiko, W. Yue, C. Jellett, M. Xiao, H.-Y. Chen, M. K. Ravva, A. H. David, A.-C. Knall, B. P. Mark Nikolka, J.-C. Flores, A. Salleo, J.-L. Bredas, H. Sirringhaus, P. Hayoz and I. McCulloch, *Nat. Commun.*, 2018, **9**, 416.
- 28 Y. K. Voronina, D. B. Krivolapov, A. V. Bogdanov, V. F. Mironov and I. A. Litvinov, *J. Struct. Chem.*, 2012, **53**, 413–416.
- 29 C. Huang, S. Barlow and S. R. Marder, *J. Org. Chem.*, 2011, **76**, 2386–2407.